

Hole concentration induced transformation of the magnetic and orbital structure in $\text{Nd}_{1-x}\text{Sr}_x\text{MnO}_3$

R. Kajimoto and H. Yoshizawa

Neutron Scattering Laboratory, I. S. S. P., University of Tokyo, Tokai, Ibaraki, 319-1106, Japan

H. Kawano*

The Institute of Physical and Chemical Research (RIKEN), Wako, Saitama 351-0198, Japan

H. Kuwahara**

Joint Research Center for Atom Technology (JRCAT), Tsukuba, Ibaraki 305-8562, Japan

Y. Tokura

*Joint Research Center for Atom Technology (JRCAT), Tsukuba, Ibaraki 305-8562, Japan
and Department of Applied Physics, University of Tokyo, Bunkyo-ku, Tokyo 113-8656, Japan*

K. Ohoyama and M. Ohashi***

Institute for Materials Research, Tohoku University, Sendai 980-77, Japan

(July 20, 2021)

In order to study the magnetic and crystal structures in the $\text{Nd}_{1-x}\text{Sr}_x\text{MnO}_3$ system, we have performed neutron diffraction measurements on melt-grown polycrystalline samples with $0.49 \leq x \leq 0.75$. As a function of hole concentration x , the system shows systematic transformation of magnetic and crystal structures, which is consistently explained by the change of the character of Mn e_g orbitals. With increasing x , the $\text{Nd}_{1-x}\text{Sr}_x\text{MnO}_3$ system exhibits a metallic ferromagnetic state, a metallic A-type AFM state, and then an insulating C-type AFM state. The CE-type charge-ordered AFM state was observed only in the vicinity of $x = 1/2$, and it coexists with the A-type AFM state for $x \gtrsim 1/2$, indicating that the energy difference between these two states is extremely small. We also found that the MnO_6 octahedra are apically compressed in the CE-type and A-type AFM states due to the $d(3x^2 - r^2)/d(3y^2 - r^2)$ or $d(x^2 - y^2)$ orbital orderings, respectively, whereas they are apically elongated by the rod-type $d(3z^2 - r^2)$ orbital ordering in the C-type AFM state. In addition, a selective broadening of Bragg peaks was observed in the C-type AFM phase, and its x dependence strongly suggests the charge ordering for a commensurate value of the hole concentration at either $x = \frac{3}{4}$ or $x = \frac{4}{5}$.

71.27.+a, 71.30.+h, 75.25.+z

I. INTRODUCTION

The systematic investigation of the phase diagram of the perovskite manganites was initiated with studies of $\text{La}_{1-x}\text{Ca}_x\text{MnO}_3$ in 1950s,^{1,2} while later in 1980s, a very similar rich phase diagram was rediscovered for the $\text{Pr}_{1-x}\text{Ca}_x\text{MnO}_3$ system.³ A distinct metallic ferromagnetic (FM) state in these phase diagrams was explained in terms of the double-exchange (DE) mechanism between the e_g electrons of Mn ions, and the richness of the phase diagrams were naturally considered as a manifestation of the strong couplings among the spin, charge, and Jahn-Teller (JT) lattice distortions.

Recent discovery of the colossal magnetoresistance (CMR) effect in doped perovskite manganites has renewed interest in these compounds, and intensive experimental and theoretical efforts have been devoted to clarify the origin of the CMR effect. In addition to the DE interactions as well as the JT distortions, recent studies revealed that the ordering of the two fold e_g orbitals

of Mn ions plays an essential role to determine physical properties in the hole-doped manganites.^{4,5,6,7,8,9} For example, it was recently reported that the underlying $d(x^2 - y^2)$ -type orbital ordering leads to a metallic anti-ferromagnetic (AFM) state instead of either the metallic FM state or a so-called CE-type charge/spin ordered insulating state. In view of newly developed ideas and of greatly improved experimental techniques, it would be extremely useful to perform systematic experimental studies concerning a phase diagram to gain further profound understanding of the interplay between e_g orbitals and magnetic as well as transport properties in doped manganites.

For a study of the hole-concentration dependent phase diagram of doped manganites, we chose the $\text{Nd}_{1-x}\text{Sr}_x\text{MnO}_3$ system, because detailed transport studies have already been performed on this system.^{10,11,12} We have carried out comprehensive neutron diffraction studies on the $\text{Nd}_{1-x}\text{Sr}_x\text{MnO}_3$ melt-grown polycrystalline samples with the Sr ion concentration of $x = 0.49$,

0.50, 0.51, 0.55, 0.60, 0.63, 0.67, 0.70, and 0.75. In what follows, we shall demonstrate that the moderately narrow one-electron bandwidth of the $\text{Nd}_{1-x}\text{Sr}_x\text{MnO}_3$ system yields a variety of physical properties such as the charge ordering, metal-insulator transition, and unique magnetic structures as a result of the interplay between the charge and/or orbital orderings and spin/lattice structures.

As a function of the hole concentration x , the $\text{Nd}_{1-x}\text{Sr}_x\text{MnO}_3$ system shows a systematic change of the magnetic structures. With increasing x , the ground state spin ordering varies from metallic ferromagnetism to charge ordered CE-type antiferromagnetism, then to metallic A-type antiferromagnetism, and finally to insulating C-type antiferromagnetism (F \rightarrow CE \rightarrow A \rightarrow C) (See Fig. 1). It can be shown that each spin order corresponds to its specific orbital order, and the determined crystal structures are consistent with the corresponding orbital order for individual AFM spin structures. For example, the structures for the CE-type and A-type AFM states are characterized by apically compressed MnO_6 octahedra, while that of the C-type AFM state consists of apically elongated octahedra, reflecting their respective layered-type or rod-type orbital ordering patterns (See Fig. 4). These systematic changes of the ordering of the spins and orbitals are well reproduced by the recent theoretical calculation which takes into account the double degeneracy of the e_g orbitals.⁵

The charge ordering also plays an important role in the $\text{Nd}_{1-x}\text{Sr}_x\text{MnO}_3$ system.^{8,10} The CE-type charge/spin order is formed in the $\text{Nd}_{1-x}\text{Sr}_x\text{MnO}_3$ system, but it is limited in a very narrow region of x around $x = 1/2$, and it coexists with the A-type AFM state in the $x = 1/2$ and $x = 0.51$ samples. The coexistence of these two states may be interpreted as the orbital-order induced phase segregation between the insulating charge-ordered state and the metallic orbital-ordered state. In the C-type AFM phase with x beyond 0.6, the Bragg peaks show a selective anisotropic broadening, which indicates disorder in the spacing of the lattice planes along the tetragonal c axis. We argue that this result indicates a possible new charge order for a commensurate hole concentration of either $x = \frac{3}{4}$ or $\frac{4}{5}$. The broadening is resulted from both the $d(3z^2 - r^2)$ -type orbital ordering and the charge ordering.

The rest of the paper is organized as follows. The next section briefly describes the experimental procedures. The experimental results are described in Sec. III, where the property of the magnetic and crystal structures in the $\text{Nd}_{1-x}\text{Sr}_x\text{MnO}_3$ system are given with the results of the Rietveld refinement analysis. In Secs. IV, the relations between the magnetic and crystal structures are discussed in detail for each type of the AFM orderings. A brief summary is given in Sec. V.

II. EXPERIMENTAL PROCEDURES

For the present study, the powder samples were prepared by powdering the melt-grown single crystals, and were pressed into rod shape. The single crystal samples were grown by floating-zone method. The detailed procedures of sample preparation were described elsewhere.^{8,13} The quality of the samples was checked by X-ray diffraction measurements and inductively coupled plasma mass spectroscopy (ICP). The results showed that the samples are in single phase and the hole concentration agrees with a nominal concentration within 1 % accuracy.

Neutron diffraction measurements were performed on a powder diffractometer HERMES and a triple axis spectrometer GPTAS installed in the JRR-3M research reactor at Japan Atomic Energy Research Institute. The incident neutron wave lengths of HERMES and GPTAS were $\lambda = 1.8196 \text{ \AA}$ and 2.35 \AA , respectively. The collimation of HERMES is $6'\text{-open-}18'$, while several combinations of the collimators were utilized at GPTAS, depending on the necessity of intensity and momentum resolution. Most of the measurements, especially those for the structural analysis, were performed on HERMES, but part of the measurements was performed with GPTAS because stronger intensity of magnetic reflections are available on this spectrometer due to the high incident neutron flux. The samples were mounted in aluminum capsules with helium gas, and were attached to the cold head of a closed-cycle helium gas refrigerator. The temperature was controlled within accuracy of 0.2 degrees. To obtain the structural parameters, the Rietveld analysis was performed on the powder diffraction data using the analysis program RIETAN.¹⁴

III. MAGNETIC AND CRYSTAL STRUCTURES

We begin with the description of the overall features of the lattice and magnetic structure of the $\text{Nd}_{1-x}\text{Sr}_x\text{MnO}_3$ system by examining the x - T phase diagram for $0.3 \leq x \leq 0.8$ shown in Fig. 1.^{11,12} In the distorted perovskite crystal structure, Mn ions are surrounded by six O ions, and the MnO_6 octahedra form pseudo-cubic lattice, whereas Nd or Sr ions occupy the body-center position of the pseudo-cubic lattice of the MnO_6 octahedra. Due to the buckling of the octahedra, however, the orthorhombic unit cell becomes $\sqrt{2} \times \sqrt{2} \times 2$ of the cubic cell. In the concentration region for $0.3 \leq x \leq 0.8$, the crystal structure is classified into two phases from the lattice parameters. The one is a well-known O' phase with $c/\sqrt{2} < b < a$,¹⁵ and appears in the lower Sr concentration region for $x \lesssim 0.55$ at room temperature, while the other is a pseudo-tetragonal O ‡ phase with $a \simeq b < c/\sqrt{2}$ for $x \gtrsim 0.55$ as indicated in the Fig. 1. At low temperatures, on the other hand, the region of the O' phase expands, and the phase boundary shifts towards around

$x = 0.60$. In addition, a monoclinic structure was detected near the low temperature structural phase boundary near $x \sim 0.60$. For $0.55 \leq x \leq 0.60$, a structural transition from the O' phase to the O^\ddagger phase coincides with the AFM transition temperature T_N .

For $x < 0.48$, the ground state is a FM metal. In the region for $0.50 \lesssim x \lesssim 0.60$, there appears a metallic AFM state with the layered type AFM ordering, which is called as A-type after Ref. 1. With further increasing x , the C-type AFM order was observed in the O^\ddagger phase. In this phase, the resistivity uniformly increases with lowering temperature, and the sample remains insulating for all temperature, although the temperature derivative of the resistivity shows an anomaly at T_N .¹² Only within a small range of the Sr concentration around $x \sim 0.50$, the system exhibits a charge-ordered insulating state which is accompanied with the CE-type AFM spin ordering after it shows the metallic FM state below T_C in the intermediate temperature region.

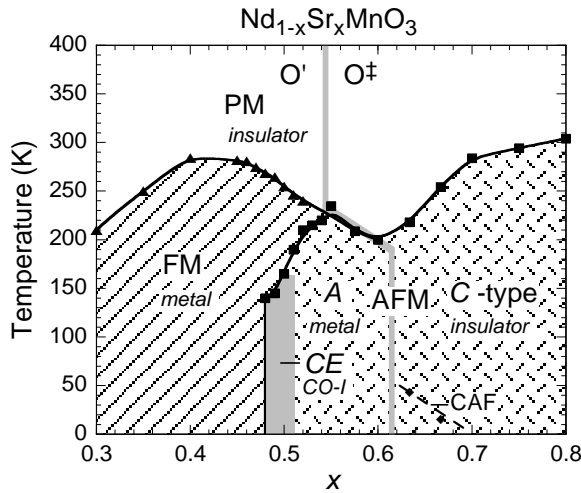


FIG. 1. Phase diagram of $Nd_{1-x}Sr_xMnO_3$.^{11,12} Each phase is denoted by capitalized labels; PM: paramagnetic insulating phase, FM: ferromagnetic order, AFM: antiferromagnetic order, CO-I: charge-ordered insulator, CE: CE-type charge/spin order, A: A-type antiferromagnetic order, C: C-type antiferromagnetic order, CAF: possible canted antiferromagnetic order.

A. Magnetic structures

The AFM spin ordering yields superlattice reflections in the neutron diffraction profiles. Since the positions of the superlattice peaks are different from each other according to the spin patterns, one can determine the spin structure from the neutron diffraction profiles. In Fig. 2, we show the typical powder diffraction patterns measured at the lowest temperature (~ 10 K) for $x = 0.49$, 0.55, and 0.75. One can clearly recognize the different superlattice reflection patterns for the CE-type, A-type, and C-type AFM spin arrangements, respectively. Cross

symbols represent the measured intensity, and solid lines are the calculated diffraction patterns for the nuclear reflections obtained by the Rietveld analysis. The AFM superlattice reflections are indicated by hatches, and the corresponding spin ordering patterns are depicted in the insets.

The CE-type spin ordering (Fig. 2(a)) is characterized by the alternate ordering of the Mn^{3+} and Mn^{4+} ions. The spin ordering pattern in the ab plane is rather complicated, and it stacks antiferromagnetically along the c axis. The magnetic reflections for the Mn^{3+} and Mn^{4+} sublattices are decoupled, and the former are indexed as $(h/2, k, l)$ with $k = \text{integer}$ and $h, l = \text{odd integer}$, while the latter are indexed as $(h/2, k/2, l)$ with $h, k, l = \text{odd integer}$.

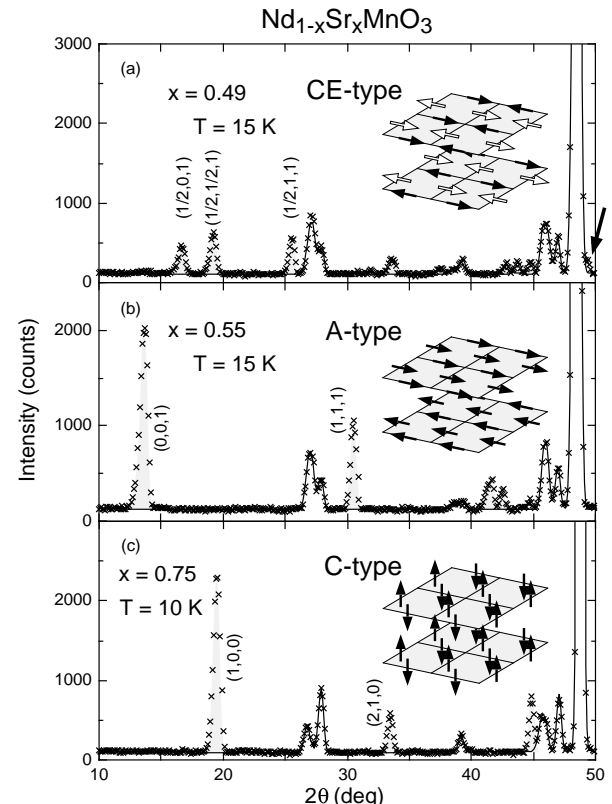


FIG. 2. Low scattering angle portion of the powder diffraction patterns for (a) $x = 0.49$ at 15 K, (b) $x = 0.55$ at 15 K, and (c) $x = 0.75$ at 10 K which were collected at HERMES. Solid lines are the calculated intensity for the nuclear reflections, and hatched peaks represent the AFM Bragg peaks. Insets are the spin patterns for each AFM structures. For the CE-type AFM structure, black and white arrows denote the spins of the Mn^{3+} and Mn^{4+} sites, respectively. A large arrow in the panel (a) indicates a superlattice peak of the lattice distortion due to the CE-type charge ordering.

In the A-type spin ordering (Fig. 2(b)), the spins order ferromagnetically in the ab plane with the moments pointing toward the a axis, and the FM planes stack antiferromagnetically along the c axis. The magnetic reflections appear at (hkl) with $h + k = \text{even integer}$ and

l = odd integer. As described later, on the other hand, we observed the monoclinic structure in the A-type AFM phase of the $x = 0.60$ sample, and the FM planes stack along the $[1\ 1\ 0]$ direction, being identical with the case of the monoclinic $\text{Pr}_{1/2}\text{Sr}_{1/2}\text{MnO}_3$.⁸

In the C-type spin ordering (Fig. 2(c)), the spins order ferromagnetically along the c axis, and the neighboring spins in the ab plane point the opposite direction. The magnetic reflections are observed at (hkl) with $h+k$ = odd integer and l = even integer.

We note that, for the $x = 0.63$ and 0.67 samples, the FM component was observed in their magnetization curve below $T_{\text{CA}} \sim 45$ K for the $x = 0.63$ sample or $T_{\text{CA}} \sim 15$ K for the $x = 0.67$ sample,¹² as indicated by the line CAF in Fig. 1. To confirm the existence of the FM component in these samples, we have measured the temperature dependence of the (110) and (002) reflections for the $x = 0.63$ polycrystalline sample. If the FM Bragg scattering appears, the intensity of these reflections should increase. Although we have observed a slight increase of the intensity below T_{CA} , its magnitude is no more than the statistical error. Even if the FM component exists, it is small to derive the accurate moment from the powder sample data.

In Table I, we summarize the magnetic moments per Mn site and their directions for all the samples studied. Interestingly, we found a clear trend that the direction of the moment is always parallel to the largest lattice constant (See Table II).

TABLE I. Magnetic structure (MS), magnetic moments, and their directions. For the CE-type AFM structure, the magnetic moments are shown for both Mn^{3+} and Mn^{4+} sites. The directions of the moments for two sites were determined to be identical within experimental accuracy.

x	T (K)	MS	Moment/Mn (μ_{B})	
0.49	15	CE	2.9, 2.6	[100]
		F	0.8 ^a	
0.50	160	F	2.6	[100]
0.51	10	CE	3.0, 2.7	[100]
0.55	10	A	2.4	[100]
	210	CE	1.7, 1.5	[100]
0.63	15	F	1.9	[100]
	10	A	3.0	[100]
0.67	10	C	2.8	[001]
0.75	12	C	2.9	[001]

^aderived from the magnetization curve in Ref. 11.

B. Crystal structures

In order to characterize the crystal structures for each phase, we have performed the Rietveld analysis on neutron powder diffraction patterns for all the samples observed at selected temperatures. The obtained structural

parameters are summarized in Table II. The types of the crystal structure (CS) and of the magnetic structure (MS) are also listed in the table. The shapes of MnO_6 octahedra for the O' and O^{\ddagger} phases are schematically illustrated in Fig. 3(a) and (b), respectively. We examine the characteristic crystal symmetry for each phase, and discuss the influence of the distortion of the MnO_6 octahedra in the following.

In spite of the fact that many orthorhombic perovskite manganites have the $Pbnm$ ($Pnma$ in another setting) symmetry due to the GdFeO_3 -type distortion, the measured powder diffraction profiles in the O' phase were well fitted with the orthorhombic space group $Ibmm$ (or $Imma$). It should be noted that the $Ibmm$ structure was also observed in $\text{Pr}_{0.65}\text{Ba}_{0.35}\text{MnO}_3$ at room temperature,¹⁶ $\text{Nd}_{0.5}\text{Sr}_{0.5}\text{MnO}_3$ (Ref. 17), and $\text{Pr}_{1/2-x}\text{Y}_x\text{Sr}_{1/2}\text{MnO}_3$ (Ref. 18). To see the difference of the two structures, the tilting of the MnO_6 octahedra for $Pbnm$ and $Ibmm$ are illustrated in Fig. 3(c). In the $Pbnm$ symmetry, the octahedra rotate both around the b and c axes. In contrast, the tilting of the octahedra is restricted only to the b axis in the $Ibmm$ symmetry, and thereby the x and y coordinates of the inplane oxygen O(2) are fixed to 1/4. As a result, two Mn–O bonds in the ab plane have an equal length.

One can distinguish the $Ibmm$ symmetry from $Pbnm$, in principle, because $Pbnm$ has a lower symmetry, and there should exist additional Bragg reflections which are allowed only in the $Pbnm$ symmetry. In the paramagnetic phase, however, we observed no additional reflection which is specific to the $Pbnm$ symmetry, and we tentatively assigned the space group in the paramagnetic phase as $Ibmm$. Unfortunately, the scattering angles of AFM superlattice reflections overlap with the $Pbnm$ specific reflections in the low temperature AFM phase, and it prevented us from determining the precise space group in this phase. Accordingly, we have performed the Rietveld analysis for both space groups, and obtained almost identical R factors. For comparison, the two parameter sets determined for both symmetries on the $x = 0.50$ sample are shown in Table II, but only the parameter sets for the $Ibmm$ symmetry are tabulated for the rest of the samples.

We found that the measured powder diffraction profiles in the O^{\ddagger} phase were well fitted with the tetragonal space group $I4/mcm$. $\text{Pr}_{0.65}\text{Ba}_{0.35}\text{MnO}_3$ at 210 K (Ref. 16) and $\text{La}_{0.5}\text{Sr}_{0.5}\text{MnO}_3$ (Ref. 19) were reported to have the same space group. The feature of the space group $I4/mcm$ is also shown in Fig. 3(d). In the $I4/mcm$ symmetry, the MnO_6 octahedra rotate only around the c axis, and all the Mn–O bonds in the ab plane are equal in length. The octahedra in the $z = 1/2$ plane rotate in the opposite directions to those in the $z = 0$ plane.

TABLE II. Lattice constants, Mn–O bond lengths, and Mn–O–Mn bond angles determined from the Rietveld analysis of the powder profiles. CS represents the types of the crystal structure and the meaning of symbols O' and O^\ddagger is described in Sec. III. The column MS gives magnetic structures for each samples: symbols P, F, CE, A, and C denote the PM, FM, CE-type AFM, A-type AFM, and C-type AFM structures, respectively. d_c and d_{ab} denote the Mn–O bond lengths along the c axis and within the ab plane. Θ_c and Θ_{ab} denote the Mn–O–Mn bond angles along the c axis and within the ab plane. For $x = 0.50$, the parameters obtained by the analysis in the $Pbnm$ symmetry are also indicated. For $x = 0.70$ at 10 K and $x = 0.75$ at 10 K, two values for $c/\sqrt{2}$ and d_c are shown because the structure parameters were analyzed according to the two phase model as described in Sec. VI-A.

x	T (K)	CS	MS	a (Å)	b (Å)	$c/\sqrt{2}$ (Å)	d_c (Å)	d_{ab} (Å)	Θ_c (°)	Θ_{ab} (°)
0.49	15	O'	CE	5.5129(3)	5.4409(3)	5.3198(3)	1.907(1)	1.9491(5)	160.9(4)	166.9(2)
	160	O'	F	5.4645(3)	5.4174(3)	5.3942(3)	1.927(1)	1.9355(6)	163.7(5)	167.4(3)
	320	O'	P	5.4727(3)	5.4286(3)	5.3978(3)	1.928(1)	1.9379(6)	163.6(5)	167.9(3)
0.50	10	O'	CE	5.5114(4)	5.4400(4)	5.3160(4)	1.906(1)	1.9481(5)	160.8(4)	167.2(3)
		in the $Pbnm$ symmetry		5.5113(4)	5.4400(4)	5.3160(4)	1.907(1)	1.92(2) 1.98(2)	160.8(4)	167.0(3)
	300	O'	P	5.4726(4)	5.4265(4)	5.3900(4)	1.927(1)	1.9370(6)	163.1(5)	168.2(3)
		in the $Pbnm$ symmetry		5.4726(4)	5.4264(4)	5.3910(4)	1.927(1)	1.93(4) 1.95(4)	163.1(4)	168.1(3)
0.51	10	O'	A+CE	5.5075(3)	5.4441(2)	5.3131(2)	1.902(1)	1.9472(4)	161.9(4)	167.7(2)
	160	O'	A	5.4999(3)	5.4446(3)	5.3242(2)	1.905(1)	1.9453(4)	162.3(4)	168.1(2)
	210	O'	F	5.4697(3)	5.4226(3)	5.3840(3)	1.923(1)	1.9358(4)	163.7(4)	168.2(3)
	300	O'	P	5.4718(3)	5.4281(3)	5.3903(3)	1.925(1)	1.9368(5)	164.0(5)	168.4(3)
0.55	15	O'	A	5.4906(3)	5.4385(3)	5.3075(3)	1.896(1)	1.9414(5)	163.6(5)	168.7(3)
	300	O^\ddagger	P	5.3903(2)	5.3903(2)	5.4999(2)	1.9445(1)	1.9218(5)	180	165.2(2)
0.60	10	M	A	5.365(2)	5.367(2)	5.4964(4)	2.01(3)	1.87(6) 1.90(6)	180	165.0(7)
						$\beta = 91.225(3)^\circ$	1.88(3)	1.92(6) 1.96(6)		166.3(7)
	300	O^\ddagger	P	5.3782(2)	5.3782(2)	5.5027(2)	1.9455(1)	1.9162(9)	180	165.8(4)
0.63	10	O^\ddagger	C	5.3236(2)	5.3236(2)	5.5633(2)	1.9669(1)	1.9009(4)	180	163.9(2)
	RT	O^\ddagger	P	5.3737(2)	5.3737(2)	5.5067(2)	1.9469(1)	1.9139(8)	180	166.1(4)
0.67	10	O^\ddagger	C	5.3190(2)	5.3190(2)	5.5588(3)	1.9653(1)	1.898(1)	180	164.4(4)
	300	O^\ddagger	P	5.3637(3)	5.3637(3)	5.5005(3)	1.9447(1)	1.9085(9)	180	167.1(5)
0.70	10	O^\ddagger	C	5.3222(3)	5.3222(3)	5.5603(4)	1.9659(1)	1.8968(5)	180	165.5(2)
						5.5387(6)	1.9582(2)			
	RT	O^\ddagger	P	5.3625(3)	5.3625(3)	5.5034(3)	1.9457(1)	1.9060(7)	180	168.2(4)
0.75	10	O^\ddagger	C	5.3243(4)	5.3243(4)	5.5432(3)	1.9598(1)	1.8944(5)	180	167.1(3)
						5.5144(4)	1.9496(2)			
	330	O^\ddagger	P	5.3717(2)	5.3717(2)	5.4843(3)	1.9390(1)	1.9053(3)	180	170.8(2)

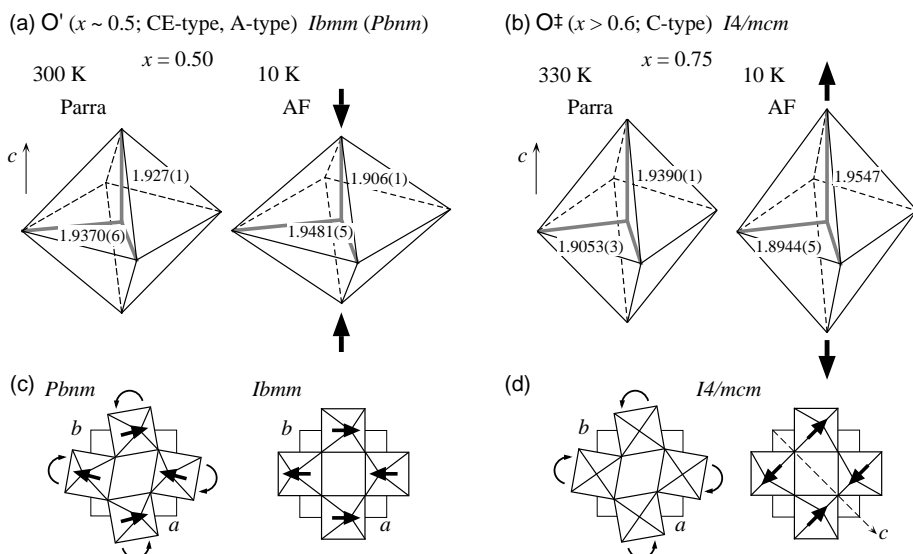


FIG. 3. Schematic picture of MnO_6 octahedra (a) in the O' phase and (b) in the O^\ddagger phase for the paramagnetic and low temperature AFM phases. (c), (d) The rotation patterns in the basal plane for designated structures. For the $I4/mcm$ structure (d), the projection of the octahedra onto the one of the $[110]$ planes is also depicted in the right panel.

As illustrated in Figs. 3(c) and (d), the observed orthorhombic and tetragonal structures are closely related. If each space group is denoted by the tiltings of the MnO_6 octahedra in the Glazer's terminology,²⁰ $Pbnm$, $Ibmm$, and $I4/mcm$ symmetries are expressed by $a^+b^-b^-$, $a^0b^-b^-$, and $a^0a^0c^-$, respectively. Here the positive and negative signs denote that the octahedra along the tilt axis are tilted in-phase or anti-phase, and 0 means no tilt.²⁰ Therefore, they can be derived from the cubic lattice by introducing successive tiltings of the MnO_6 octahedra. Comparing the projection of the octahedra onto the [001] plane in the orthorhombic phase (Fig. 3(c)) and that onto the [110] plane in the tetragonal phase (right part of Fig. 3(d)), one can see that, as far as the tilting of the octahedra is concerned, the tetragonal axis [001] coincides with the [110] axis in the orthorhombic structure.

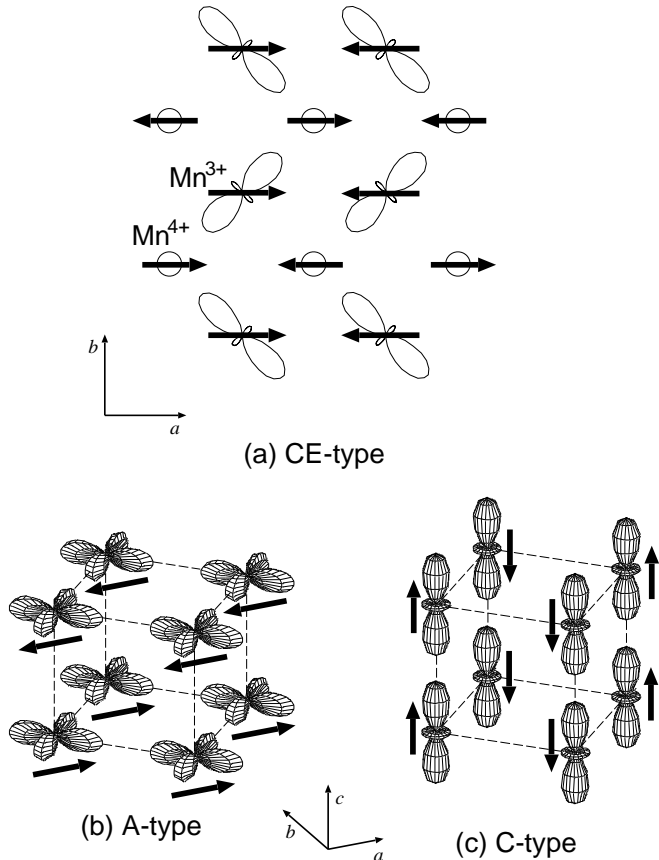


FIG. 4. Schematic picture of the orderings of the e_g orbitals in AFM phases. (a) CE-type, (b) A-type, and (c) C-type, respectively. The directions of the spins are represented by arrows.

In addition to the tilting of octahedra, distortions of the MnO_6 octahedra provide useful information on the orbital as well as charge orderings. As one can see from Table II, the two Mn–O bonds in the ab plane are always longer than those along the c axis in the O' phase. This feature indicates that the A-type AFM structure

is accompanied with the $d(x^2 - y^2)$ type orbital order as depicted in Fig. 4(b), and this result is supported by the recent theoretical calculations.⁵ The $d(x^2 - y^2)$ type orbital order causes a unique magnetic and transport properties due to the strongly anisotropic couplings within and perpendicular to the orbital ordered planes. As we have predicted and demonstrated in the preceding studies,^{8,11,12,24,27} and will be discussed in Sec. V, this type of orbital order yields an *metallic* A-type AFM state. It should be noted that one might consider that the orbital-order-induced anisotropy will be less significant in the paramagnetic phase, since the difference of the bond length between the apical and inplane Mn–O bonds becomes rather small at elevated temperatures. Surprisingly, however, the anisotropic behavior persists in high temperature phases. Very recently, we have demonstrated the existence of the anomalous anisotropic spin fluctuations in the paramagnetic and FM phases in $\text{Nd}_{0.50}\text{Sr}_{0.50}\text{MnO}_3$,⁹ indicating that the $d(x^2 - y^2)$ type orbital order has strong influence at high temperatures.

In the O' phase, on the other hand, the Mn–O bond length along the c axis is longer than the ones in the ab plane, and this difference is further enhanced in the AFM phase. The apically stretched MnO_6 octahedron is consistent with the ordering of the $d(3z^2 - r^2)$ orbitals depicted in Fig. 4(c). It is worth to mention that the recent theoretical calculation confirmed that there appears the C-type AFM state with the ordering of the $d(3z^2 - r^2)$ orbitals in the higher doping region.⁵

Finally, we would like to mention the CE type charge/orbital ordering. The CE-type ordering is characterized by the alternate ordering of the Mn^{3+} and Mn^{4+} ions and by the ordering of the $d(3x^2 - r^2)/d(3y^2 - r^2)$ orbitals on the Mn^{3+} sites in the ab plane as depicted in Fig. 4(a). This type of orbital ordering doubles a size of the unit cell along the b axis, and produces the superlattice reflections at $(h, k/2, l)$ with $h = \text{even}$, $k = \text{odd}$, and $l = \text{integer}$. Even for the polycrystalline samples, we could observe the superlattice reflections in the $x = 0.49$ and 0.50 samples at $2\theta = 49^\circ$ (indicated by an arrow in Fig. 2(a)) which can be indexed as $(2\frac{1}{2}2) + (2\frac{3}{2}0)$, as was the case of the $\text{Pr}_{1-x}\text{Ca}_x\text{MnO}_3$ system.³ On the other hand, this type of charge ordering necessitates to consider two independent Mn sites for the Mn^{3+} and Mn^{4+} ions. Namely we need to treat two types of distortions in the MnO_6 octahedra. Clearly, such an analysis multiplies the number of parameters in a fitting process, and would yield less reliable structural parameters. For this reason, we omitted to treat the doubling of the unit cell due to the orbital ordering, and performed the Rietveld analysis on the CE-type samples assuming only the original $Ibmm/Pbnm$ structure. Consequently, the obtained Mn–O bond lengths and Mn–O–Mn angles give the averaged values for two Mn sites.

IV. INFLUENCE OF THE CE-TYPE ORDERING

Near $x \sim \frac{1}{2}$, the doped perovskite manganites are usually expected to show a so-called CE-type charge/orbital/spin superstructure depicted in Fig. 4(a).^{1,2,3} For the $\text{Pr}_{1-x}\text{Ca}_x\text{MnO}_3$ system, for instance, the CE-type ordering is observed over a wide range of $0.3 \lesssim x \leq 0.5$.^{3,21,22,23} As shown in Fig. 1, however, the CE-type ordering is observed only in a very limited range near $x \sim 0.50$ in the $\text{Nd}_{1-x}\text{Sr}_x\text{MnO}_3$ system. Note that, the CE-type ordering was not observed in the $x = 0.55$ sample.⁸

A distinct feature of the CE-type ordering in the $\text{Nd}_{1-x}\text{Sr}_x\text{MnO}_3$ system is the coexistence with another spin ordering. Because the FM order is taken over by the A-type AFM order near $x = 0.5$ in the $\text{Nd}_{1-x}\text{Sr}_x\text{MnO}_3$ system (See the phase diagram in Fig. 1.), the FM order coexists with the CE-type order in the $x = 0.49$ sample, whereas the A-type AFM order coexists with the CE-type order in the $x = 0.51$ sample. To illustrate the situation more specifically, we shall describe the behavior of the $x = 0.49$ and 0.51 samples in detail below. Concerning the AFM side for $x > 0.50$, similar results were reported very recently on the same $\text{Nd}_{1-x}\text{Sr}_x\text{MnO}_3$ system with $x = 0.52$ and 0.54 .²⁵

Figure 5(a)–(f) show the temperature dependences of the magnetic Bragg peaks, the lattice constants, and the resistivity for the $x = 0.49$ and 0.51 samples. In the $x = 0.49$ sample, the FM spin ordering was observed below $T_C \simeq 280$ K. As shown in Fig. 5(a), the intensity of the (110) and (002) reflections increases below $T_C \simeq 280$ K due to the FM order. Below $T_N \simeq 160$ K, it suddenly drops, and the $(\frac{1}{2}\frac{1}{2}1)$ reflection appears, indicating the formation of the CE-type AFM order. It should be noted, however, that the magnetization study strongly suggests the persistence of the ferromagnetic order below T_N . As shown in Table I, the $x = 0.49$ sample has the FM moment of $0.8\mu_B$ at 15 K. Therefore, the FM order coexists with the CE-type AFM order in the $x = 0.49$ sample.

In the $x = 0.51$ sample, the behavior of the magnetic ordering was very similar to that of the $x = 0.50$ sample reported in Refs. 8 and 9. As shown in Fig. 5(d), the intensity of the (110) + (002) reflections increases below $T_C \simeq 240$ K owing to the onset of the FM order. With decreasing temperature, it increases quickly, but shows a sudden drop at $T_N^A \simeq 200$ K at which the (001) A-type AFM reflection appears. In contrast to the $x = 0.49$ FM sample, the intensity of (110) + (002) reflection in the $x = 0.51$ AFM sample has no magnetic contribution below T_N^A . The difference between the intensity above T_C and below T_N^A is due to the structural transition at T_N^A . With further lowering temperature, the $(\frac{1}{2}\frac{1}{2}1)$ CE-type AFM superlattice reflection appears below $T_N^{\text{CE}} \simeq 150$ K. Note that the CE-type ordering suppresses the increase of the intensity of the (001) A-type AFM reflection below T_N^{CE} , indicating that the two spin orderings are strongly

correlated.

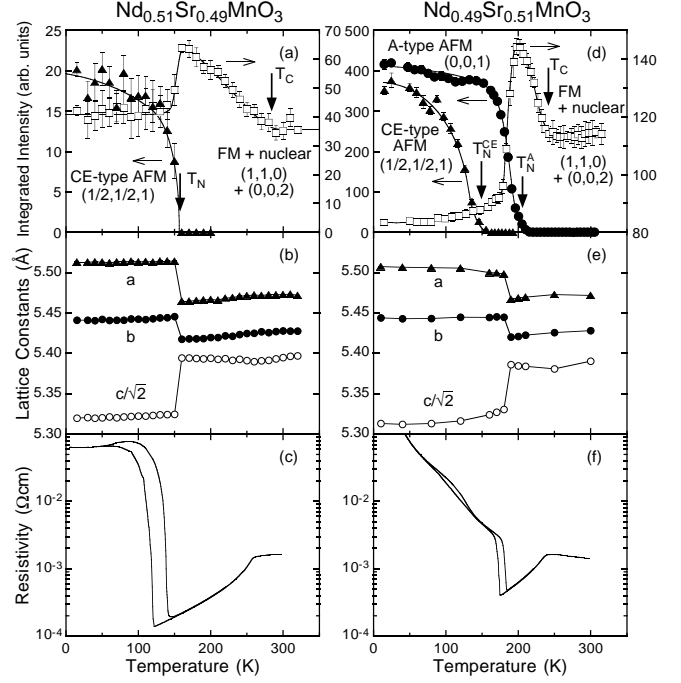


FIG. 5. Temperature dependence of the intensities of the magnetic Bragg peaks, the lattice constants, and the resistivity for the $x = 0.49$ FM sample: ((a)–(c)), and for the $x = 0.51$ AFM sample: ((d)–(f)), respectively. The resistivity data are reproduced from Ref. 12

The temperature dependence of the lattice constants in the $x = 0.49$ sample is shown in Fig. 5(b). It shows a weak inflection at T_C , while a sharp jump at T_N , where the c axis shrinks while the a and b axes expand, being consistent with the CE-type orbital ordering in the ab plane. Similarly, the lattice constants of the $x = 0.51$ AFM sample exhibit a large split at T_N^A (Fig. 5(e)), indicating that the A-type magnetic transition is accompanied with the structural transition which stabilizes the $d(x^2 - y^2)$ -type planar orbital ordering as discussed in the previous section. They show, however, no distinct anomaly at T_N^{CE} . In fact, we have carried out detailed structural analysis on the two powder diffraction data, one is observed at $T = 160$ K in the A-type AFM phase for $T_N^{\text{CE}} < T < T_N^A$ and the other at $T = 10$ K in the low temperature phase where two orderings coexist. But we found no difference of crystal structure between two AFM phases (see Table II). In particular, all the nuclear reflections in the powder diffraction data at 10 K can be well fitted to a single structure in spite of the coexistence of the A-type and CE-type AFM orderings. These results on the $x = 0.51$ sample demonstrate that the crystal structure of the A-type AFM phase in $\text{Nd}_{1-x}\text{Sr}_x\text{MnO}_3$ is practically indistinguishable from that of the CE-type phase despite the difference of spin structure.²⁶

The change of the magnetic structure also has a strong

influence on the behavior of the resistivity. As shown in Fig. 5(c), the resistivity in the $x = 0.49$ FM sample shows the metallic behavior below T_C , then a sharp rise at T_N due to the CE-type charge order. The increase of the resistivity is, however, suppressed below ~ 100 K by the FM order with the moments of $0.8\mu_B$ which coexists with the CE-type AFM spin order. In the $x = 0.51$ AFM sample, on the other hand, the resistivity shows the metallic behavior below T_C , a moderate increase at the onset of the A-type AFM spin order, and it shows the second increase at T_N^{CE} due to the CE-type charge order as shown in Fig. 5(f). By comparing this behavior with that of the $x = 0.49$ FM sample, the influence of the spin ordering is clear. The FM spin order restricts the resistivity of the $x = 0.49$ FM sample at the order of $\rho \sim 5 \times 10^{-2} \Omega\text{cm}$ for $T < T_N$. In contrast, the resistivity of the $x = 0.51$ sample exhibits a jump at T_N^{A} , it remains an order of $\rho \sim 5 \times 10^{-3} \Omega\text{cm}$ in the metallic A-type AFM phase for $T_N^{\text{CE}} < T < T_N^{\text{A}}$, and then increases monotonically below $T < T_N^{\text{CE}}$. It should be noted that the metallic resistivity of the $x = 0.51$ AFM sample in the A-type AFM state for $T_N^{\text{CE}} < T < T_N^{\text{A}}$ is of the same order with those of other *metallic* A-type AFM samples.^{8,9,11,12,27}

There are several possibilities for the origin of the simultaneous presence of the CE-type ordering with the FM or A-type AFM spin orderings in the $x = 0.49$ and 0.51 samples. Scenarios of the inhomogeneous distribution of the holes in the sample or a canted magnetic ordering consisting of the CE-type and A-type moments seem to be consistent with observed results. The former scenario can be attributed either to a trivial concentration distribution, or to an intrinsic phase segregation. Although it is extremely difficult to experimentally distinguish these two possibilities, there are some interesting observations which seem to favor the intrinsic spontaneous phase segregation in doped manganites near $x \sim \frac{1}{2}$.

As mentioned above, the increase of the CE-type Bragg intensity suppresses the A-type AFM intensity in the $x = 0.51$ sample; in other words, the CE-type order grows at the expense of the A-type ordered region. This fact excludes the possibility of a trivial distribution of the hole concentration. In addition, we found that the magnetic moments for the A-type and CE-type AFM structures lie in the same direction, i.e., along the a axis (Table I). This result seems to suggest that a canted magnetic ordering is unlikely in the present case.²⁸

We also found that the averaged lattice structure of the CE-type phase is almost identical with that of the A-type phase in the present samples. As shown in the case of the $x = 0.51$ sample, the lattice parameters exhibit little anomaly between two phases. Since both phases exhibit the orbital ordering within the basal plane, when the charges are progressively localized with decreasing T , the orbitals are reorganized with surprisingly small lattice distortions from the $d(x^2 - y^2)$ -type orbital order for the A-type AFM ordering to the $d(3x^2 - r^2)/d(3y^2 - r^2)$ -type orbital order for the CE-type ordering.

Combining these observations, we believe that the simultaneous existence of two states strongly indicates that these two states are very close in energy, and their relative fraction can be easily varied either by temperature or by tuning other physical parameters such as one electron bandwidth, and at the same time this could explain why the CE-type ordering appears only in a very narrow concentration range of $1 \sim 2\%$ around the $x = 1/2$ in the $\text{Nd}_{1-x}\text{Sr}_x\text{MnO}_3$ system. As discussed in Ref. 30, we argue that this behavior can be viewed as an effective phase separation between two different orbital ordered regions which takes place in doped manganites with hole concentration $x \gtrsim \frac{1}{2}$. The strong correlation between the coexistence of the CE-type and A-type orderings and their resistivity is recently pointed out for doped manganite systems with $x = \frac{1}{2}$ including two-dimensional single and bilayer systems, $\text{La}_{0.5}\text{Sr}_{1.5}\text{MnO}_4$ and $\text{La}_1\text{Sr}_2\text{Mn}_3\text{O}_7$ (Ref. 30).

V. METALLIC A-TYPE ANTFERROMAGNET

The most important result in the metallic A-type antiferromagnetic phase is the fact that all crystal structures in this phase share the common feature that the lattice spacing in the direction of the AFM stacking is the smallest (See Fig. 3). This salient feature causes an anisotropy in both magnetic and transport properties, as discussed in Sec. III-B. As reported recently, the spin wave dispersion relation in the metallic A-type AFM $\text{Nd}_{0.45}\text{Sr}_{0.55}\text{MnO}_3$ exhibits a large anisotropy of the effective spin stiffness constants between the intraplanar direction within the FM layers and the interplanar direction perpendicular to the layers.^{8,27} It should be noted that a similar directional anisotropy of the resistivity was also observed in the A-type AFM samples.^{11,12} These anisotropies in physical properties are strong evidence of the $d(x^2 - y^2)$ -type orbital ordering within the FM layers, and are fully consistent with the characteristics of the crystal and magnetic structures observed in the present studies. In this section, we will focus on the detailed crystal structures observed in the region of $0.55 \leq x < 0.63$ where the system shows a transition from the paramagnetic O^\ddagger phase to the metallic A-type AFM O' phase.

Figures 6 (a) and (b) show the temperature dependences of the A-type AFM Bragg peak and the d spacing of the planes of the (110)/(002) doublet for the $x = 0.55$ sample. The (001) A-type AFM Bragg peak appears below $T_N = 230$ K. The lattice spacings of the (002) and (110) nuclear reflections cross at T_N due to the change of the space group from O^\ddagger to O' . The shrinkage of the c axis in the A-type AFM phase reflects the $d(x^2 - y^2)$ -type orbital ordering.

Figures 6(c) and (d) show the similar temperature dependences for the $x = 0.60$ sample. This sample also belongs to the tetragonal O^\ddagger phase at the paramagnetic phase, and shows a first order structural phase transi-

tion at T_N . In contrast to the $x = 0.55$ sample, however, it has a monoclinic structure whose unique axis is the c axis in the AFM phase, as one can clearly see the splitting of the tetragonal (220) reflection into the monoclinic (220) + (220) reflections below T_N .

We have previously reported that $\text{Pr}_{0.50}\text{Sr}_{0.50}\text{MnO}_3$ also has the monoclinic structure in the A-type AFM phase, and its crystal structure belongs to the $P112_1/n$ ($P2_1/c$, cell choice 2) space group.⁸ In order to analyze the powder patterns of the present $\text{Nd}_{0.40}\text{Sr}_{0.60}\text{MnO}_3$ sample collected at 10 K, we have performed the Rietveld analysis assuming the same $P112_1/n$ space group at first. However, we noticed that the $P112_1/n$ space group predicts too many allowed reflections, compared to the observed Bragg peaks. Therefore, in the next step, we fitted the profile with the space group $I112/m$ ($C2/m$, cell choice 3) which has a higher symmetry, and we found that the fitting yields the almost equal goodness with the case of the $P112_1/n$ space group. We have listed the parameters obtained with this symmetry in Table II. The difference of the crystal structure of two space groups are the following: In both space groups, two unequal Mn sites are placed at adjacent sites alternately in all directions, but the freedom of the O sites is much restricted in the case of the $I112/m$ structure. The apical oxygen O(1) is placed on the line which connect the nearest Mn ions along the c axis, and only its z coordinate is allowed to vary, while the position of the inplane oxygen O(2) and O(3) are confined in the ab plane.

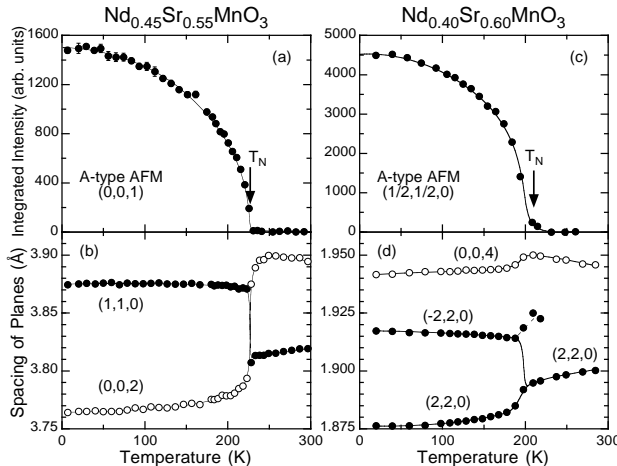


FIG. 6. Temperature dependence of the intensities of the AFM Bragg peaks and the spacings of the lattice planes. (a),(b) (001) AFM Bragg peak and the spacing of (110) and (002) planes for $x = 0.55$. (c),(d) the $(\frac{1}{2},\frac{1}{2},0)$ AFM Bragg peak and the spacing of (220) and (004) planes for $x = 0.60$.

Unfortunately, the error of the refinement for the $x = 0.60$ sample is the worst among the samples analyzed in the present study ($S = R_{\text{wp}}/R_{\text{e}} \simeq 2.2$ for the $x = 0.60$ sample, whereas S is less than 2 for other samples). The main reason for the large R factor may be that this sample is not in a single phase at 10 K, presumably because

the AFM phase of $x = 0.60$ lies just at the boundary between the orthorhombic O' region and the tetragonal O ‡ region.³¹ For the $x = 0.63$ sample, we found that $\sim 10\%$ of the sample of the $x = 0.63$ sample has the same lattice constants with those of the $x = 0.60$ sample at 10 K, and shows the A-type antiferromagnetism.

This large R factor causes slight ambiguity in identification of the indices for the closely located peaks such as (004), (220), and (220) in the monoclinic phase, but when the assignment of the three axes were assumed as labeled in Fig. 6(d), the Rietveld analysis gave the best fit.

The $x = 0.60$ sample exhibits the same A-type AFM structure with the $x = 0.51$ and 0.55 samples. However, the monoclinic structure in the $x = 0.60$ sample affects its magnetic structure. The AFM superlattice reflections in the $x = 0.60$ sample are indexed as $\mathbf{Q} = (2n \pm \frac{1}{2}, 2n' \pm \frac{1}{2}, \text{even})$ with $n, n' = \text{integer}$, while those in the $x = 0.51$ and 0.55 samples are indexed as (hkl) with $h+k = \text{even integer}$ and $l = \text{odd}$. This difference of the reflection conditions indicates that the propagation vector of the AFM structure for $x = 0.60$ is different from the other A-type samples. It is rotated by 90° from the [001] axis, and it points towards the [110] direction. This is consistent with the fact that the d spacing of (001) remains larger than that of (110) below T_N in this sample. Such a rotation of the propagation vector of the A-type AFM ordering was also observed in another monoclinic sample $\text{Pr}_{0.50}\text{Sr}_{0.50}\text{MnO}_3$ (Ref. 8).

VI. POSSIBLE CHARGE ORDER IN THE C-TYPE AFM INSULATING PHASE

Finally, we shall discuss the features of the insulating C-type AFM state which appears in the O ‡ phase for $x \geq 0.63$.

A. anomaly in the lattice constant c in the C-type AFM phase

Figure 7 shows the temperature dependences of the intensity for the AFM Bragg peak and of the lattice constants for the $x = 0.75$ sample. The (100) AFM Bragg peak for the C-type spin ordering was observed below $T_N \simeq 300$ K. The change of the lattice constants with temperature is very smooth throughout T_N , although the difference between the values at 330 K and those at 10 K is quite large. With lowering temperature, the length of the c axis increases whereas the a (b) axis decreases.

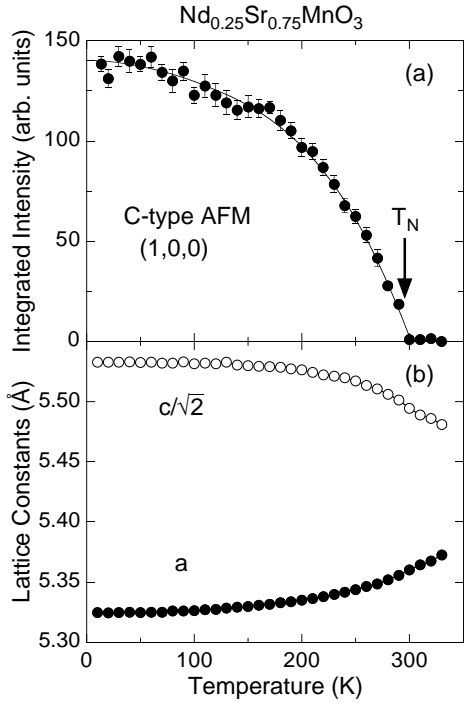


FIG. 7. Temperature dependence of the intensities of the AFM Bragg peaks and the lattice constants for $x = 0.75$.

We would like to stress that we have observed a selective broadening of the nuclear Bragg reflections. Figure 8 represents the temperature dependence of the peak widths (FWHM) of the (004) and (220) reflections for $x = 0.75$, 0.70, and 0.67. The width of the (220) reflection remains constant throughout all temperatures. However, it is clear that the width of the (004) peak gradually increases below $T \sim T_N$. Note that the (004) reflection is attributed solely to nuclear reflection, and no magnetic scattering contributes to this reflection for the C-type AFM order (see Table I). Comparing the data for three samples depicted in Fig. 8, one can see that the $x = 0.75$ sample shows the most clear broadening, and it becomes less distinct as x decreases.

In order to clarify the origin of the broadening of the nuclear Bragg reflections, we have examined the powder diffraction patterns and have found that the broadening was limited to the reflections with the Miller indices (hkl) of large l , for example, (004), (114), (206), (226), and (008). In Fig. 9, we show typical examples of the broadening of the Bragg profiles for the $x = 0.75$ sample at 10 K. Filled circles are the observed intensity profiles, and solid lines are the calculated intensity obtained by the Rietveld refinement. One can clearly see that the widths of the (004) and (206) reflections are wider than those of (220) and (422). We first fitted the profile assuming that the sample is in a single phase with the $I4/mcm$ symmetry, and the calculated profiles are depicted in Figs. 9(a) and (b). Despite the fitting is quite good for (220) and (422), the fit to (004) and (206) is relatively poor.

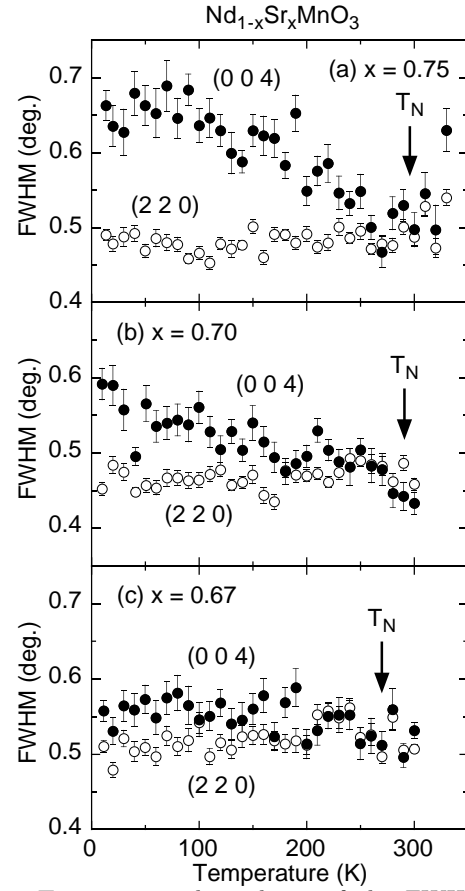


FIG. 8. Temperature dependence of the FWHM of the (004) and (220) reflections for (a) $x = 0.75$, (b) $x = 0.70$, and (c) $x = 0.67$.

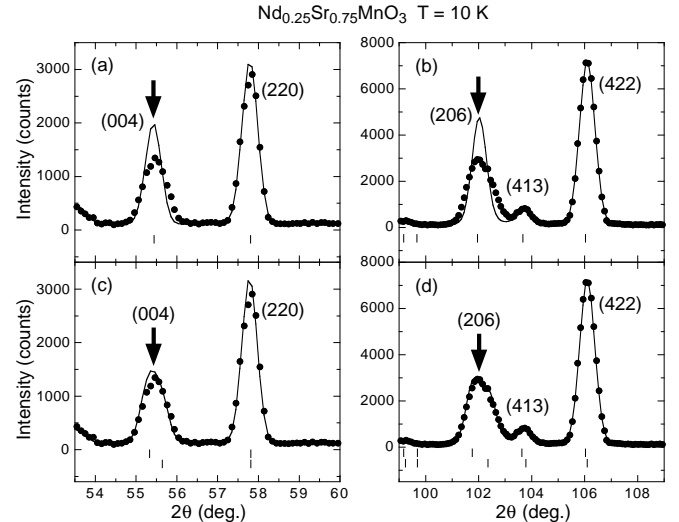


FIG. 9. Portions of the powder diffraction pattern of the $x = 0.75$ sample at 10 K. Solid lines represent the calculated intensity obtained by the Rietveld analysis. Calculated peak positions are indicated as vertical bars. (a), (b) The refinement was performed with single phase of the space group $I4/mcm$. (c), (d) The refinement was performed with two phase model described in the text.

Because the calculated peak positions are in excellent agreement with the observed peaks, the symmetry $I4/mcm$ assumed in the analysis cannot be too far from the true crystal symmetry. Therefore, one of the possible reasons for these broadening could be the lowering of the symmetry to the orthorhombic or monoclinic one, and the resultant splitting of the original reflections which may be unresolved due to the moderate angular resolution of the neutron powder diffractometer. This possibility, however, will be easily discarded because the peak broadening is also observed at $(00l)$ reflections which will split in neither the orthorhombic nor monoclinic structure.

Considering the fact that the peak broadening occurs selectively at the reflections with large l , that is, the reflections from the lattice planes which are nearly perpendicular to the c axis, it is very likely that it is originated from an anisotropic strain in the system, and a possible microscopic picture of such a strain is a distribution of the lattice constant of the c axis. To ascertain this idea, we have assumed a simple structural model that the sample consists of two phases in which they have two different lattice constants for the c axis. By keeping other parameters identical for both phases, we have fitted the observed diffraction pattern to this model, and have obtained substantially improved results as depicted in Figs. 9(c) and (d).

From these facts, we concluded that the observed selective broadening of Bragg peaks results from the anisotropic strain caused by a distribution of the $d(3z^2 - r^2)$ orbitals. As stated above, the e_g electrons occupy the $d(3z^2 - r^2)$ orbitals in the O^\ddagger phase. When the charges are localized in the insulating phase, only Mn^{3+} sites have the $d(3z^2 - r^2)$ orbital, and Mn^{4+} sites have no e_g electrons. In Fig. 10, we illustrated an arrangement of Mn^{3+} with the $d(3z^2 - r^2)$ orbital and Mn^{4+} with no e_g orbital. Because the $d(3z^2 - r^2)$ orbital extends toward the c direction, the distance between Mn^{3+} and Mn^{4+} are elongated along the c direction, whereas in the ab plane the Mn^{3+} – Mn^{4+} distance is almost equal to the Mn^{4+} – Mn^{4+} distance. At high temperatures, the charges are mobile by thermal activation, which averages out the local distortion of the lattice spacing along the c axis. At low temperatures, on the other hand, the thermal energy is insufficient for the charges to hop, and the local ordering of the e_g electrons with the $d(3z^2 - r^2)$ orbital may be formed, and it leads to the anomaly in the lattice constant. It should be noted that the broadening of the peak starts below T_N where the C-type AFM spin ordering is formed as shown in Fig. 8, and at the same time a temperature derivative of the resistivity shows an anomaly.¹²

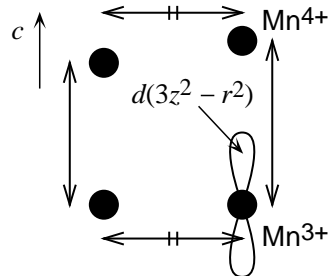


FIG. 10. Schematic picture about the relation of e_g orbital ordering and the lattice spacing in the O^\ddagger phase.

B. possibility of the $x = 0.8$ charge ordering in the C-type AFM phase

As we described in the previous subsection, we found that the broadening of the nuclear Bragg peaks becomes clearer as x increases, indicating that the charge localization/ordering is also progressively stabilized with the increase of x . Furthermore, the anomaly of the temperature derivative of the resistivity at T_N develops as x increases, and it is most clearly observed at $x = 0.80$. In addition, the resistivity of the $x = 0.80$ sample itself shows a steep increase at T_N with decreasing temperature.¹² Judging from these facts, it is very likely that the charge ordering associated with the $Mn^{3+} : Mn^{4+}$ ratio of 1 : 4 is formed below T_N . On the other hand, Jirák *et al.* was reported that superlattice reflections which might be originated from the charge ordering of $Mn^{3+} : Mn^{4+} = 1 : 3$ were observed in their $Pr_{0.2}Ca_{0.8}MnO_3$ sample whose valence distribution of the Mn ions was determined to be $Mn_{0.25}^{3+}Mn_{0.75}^{4+}$ by chemical analysis.³ To check a possibility of such charge ordering, we examined our powder pattern profiles in detail, but it was not possible to detect any indication of the superlattice reflections for the charge ordering in the powder diffraction data. A study of a single crystal sample is strongly desirable to elucidate the nature of a possible 4/5 or 3/4 charge ordering in the C-type AFM phase.

As for the charge ordering for $x \geq 1/2$, an interesting charge ordering with large periodicity was recently observed in the $La_{1-x}Ca_xMnO_3$ system.^{32,33,34,35,36} In this system, incommensurate superlattice peaks were observed at the wave vector $Q = (\delta, 0, 0)$ with $\delta \sim 1 - x$ below the charge ordering temperature T_{CO} by electron diffraction. To understand the incommensurability, a stripe-type charge/orbital ordering was proposed.^{4,35,36} In this model, a pair of $Mn^{3+}O_6$ stripes are formed, and they are separated by another stripe-shaped region of the $Mn^{4+}O_6$ octahedra. A pair of $Mn^{3+}O_6$ stripes are accompanied with the $d(3x^2 - r^2)/d(3y^2 - r^2)$ orbital ordering and with a large lattice contraction due to the JT effect, while the $Mn^{4+}O_6$ regions are free from lattice distortions. At $x = 1/2$, this incommensurate pairs of JT stripes converges to the well-known CE-type orbital/spin ordering. Similar incommensurate superlattice peaks were also observed in $Bi_{1-x}Ca_xMnO_3$ single

crystals with $0.74 \leq x \leq 0.82$,³⁷ while the long-period structure with four-fold periodicity (21 Å) and 32-fold periodicity (170 Å) to the orthorhombic lattice unit were clearly observed in the $x = 0.80$ sample.³⁸ These results also share many features with the paired JT stripes proposed for the $\text{La}_{1-x}\text{Ca}_x\text{MnO}_3$ with $x \gtrsim 0.5$.

We would like to point out that this type of paired JT stripe ordering can be easily excluded from the possible charge ordering for the present C-type AFM $\text{Nd}_{1-x}\text{Sr}_x\text{MnO}_3$ samples from the consideration of the lattice parameters. For the CE-type charge ordering and associated paired JT stripe ordering, the orthorhombic c axis (in the $Pbnm$ notation) must be the shortest. This is due to the fact that the $d(3x^2 - r^2)/d(3y^2 - r^2)$ orbitals lie in the ab plane as shown in Fig. 4, and it is easily checked that this relation is satisfied by other manganites with the CE-type ordering, for example, $\text{Pr}_{1-x}\text{Ca}_x\text{MnO}_3$ (Refs. 3, 21, 39) as well as $\text{La}_{1-x}\text{Ca}_x\text{MnO}_3$ with $x \geq 0.50$ (Refs. 1, 40, 41) from the lattice constants data in the existing reports.

On the other hand, the c axis is the longest for the C-type AFM spin ordering in the present $\text{Nd}_{1-x}\text{Sr}_x\text{MnO}_3$, in the C-type AFM region of $\text{Pr}_{1-x}\text{Ca}_x\text{MnO}_3$ (Ref. 3) and in $\text{La}_{0.2}\text{Ca}_{0.8}\text{MnO}_3$ (Ref. 1). As explained in the previous subsection, this relation of the lattice parameters results from the $d(3z^2 - r^2)$ -type orbital ordering in the C-type structure. Concerning the magnetic ordering of the $\text{Bi}_{1-x}\text{Ca}_x\text{MnO}_3$ system, we are puzzled that the magnetic ordering was reported to be of C-type.³⁷ Because the c axis ought to be the longest for the C-type spin order, it cannot be compatible with the proposed JT stripe-type ordering with the shortest c axis.

Finally, we comment that the FWHM of the (004) peak of the $x = 0.75$ sample at 330 K is larger than the one at about 300 K (see Fig. 8). This is because a finite amount of the scattering exists between the (220) and (004) peaks. Similar extra scattering is observed at some other scattering angles. Presumably, another phase with very close length of the a and c axis may exist at higher temperatures, and the remnant of the higher T phase may exist at 330 K.

VII. CONCLUSIONS

Neutron diffraction study was performed on $\text{Nd}_{1-x}\text{Sr}_x\text{MnO}_3$ powder samples with $0.49 \leq x \leq 0.75$ and their crystal and magnetic structure were analyzed by the Rietveld method. A systematic change of the crystal and magnetic structures was observed as a function of x . With increasing x , the magnetic structure of the ground state varies from metallic ferromagnetism to charge ordered CE-type antiferromagnetism, then to metallic A-type antiferromagnetism, and finally to insulating C-type antiferromagnetism. The magnetic structure is driven by underlying Mn e_g orbital ordering and resultant crystal structure. In the CE-type

and A-type AFM states, the crystal structure is characterized by apically compressed MnO_6 octahedra reflecting the planar $d(x^2 - y^2)$ -type orbital ordering. On the other hand, in the C-type AFM state it consists of apically elongated octahedra which is influenced by the ordering of the rod-type $d(3z^2 - r^2)$ orbitals.

The CE-type AFM state was observed only in the neighborhood of $x = 1/2$. In the $x = 0.51$ sample, the CE-type AFM state and the A-type AFM state coexisted due to the small energetic difference between the two AFM states. In addition, the C-type AFM phase exhibits an anisotropic broadening of Bragg peaks, which becomes clearer as x increases. This can be interpreted as a precursor of the $d(3z^2 - r^2)$ -type orbital ordering at $\text{Mn}^{3+} : \text{Mn}^{4+} = 1 : 3$ or $1 : 4$.

ACKNOWLEDGMENTS

This work was supported by a Grand-In-Aid for Scientific Research from the Ministry of Education, Science, Sports and Culture, Japan and by the New Energy and Industrial Technology Development Organization (NEDO) of Japan.

* present address: Solid State Division, Oak Ridge National Laboratory, Oak Ridge, Tennessee 37831.

** present address: Faculty of Science and Technology, Sophia University, Chiyoda-ku, Tokyo 102-8554, Japan.

*** present address: Faculty of Engineering, Yamagata University, Yonezawa, Yamagata 990-8510, Japan.

¹ E. O. Wollan and W. C. Koehler, Phys. Rev. **100**, 545 (1955).

² J. B. Goodenough, Phys. Rev. **100**, 564 (1955).

³ Z. Jirák, S. Krupička, Z. Šimša, M. Dlouhá, and S. Vratislav, J. Magn. Magn. Matt. **53**, 153 (1985).

⁴ S-W. Cheong and C. H. Chen, *Colossal Magnetoresistance, Charge Ordering and Related Properties of Manganese Oxides* ed. by C. N. R. Rao and B. Raveau (World Scientific, 1998), pp. 241.

⁵ R. Maezono, S. Ishihara, and N. Nagaosa, Phys. Rev. B **57**, R13993 (1998); R. Maezono, S. Ishihara, and N. Nagaosa, Phys. Rev. B **58**, 11583 (1998).

⁶ T. Mizokawa and A. Fujimori, Phys. Rev. B **56**, R493 (1997).

⁷ W. Koshiba, Y. Kawamura, S. Ishihara, S. Okamoto, J. Inoue, and S. Maekawa, J. Phys. Soc. Jpn. **66**, 957 (1997).

⁸ H. Kawano, R. Kajimoto, H. Yoshizawa, Y. Tomioka, H. Kuwahara, and Y. Tokura, Phys. Rev. Lett. **78**, 4253 (1997); H. Kawano, R. Kajimoto, H. Yoshizawa, J.A. Fernandez-Baca, Y. Tomioka, H. Kuwahara, and Y. Tokura, Physica B **241-243**, 289 (1998).

⁹ H. Kawano, R. Kajimoto, H. Yoshizawa, Y. Tomioka, H. Kuwahara, and Y. Tokura, cond-mat/9808286.

¹⁰ H. Kuwahara, Y. Tomioka, A. Asamitsu, Y. Moritomo, and Y. Tokura, *Science* **270**, 961 (1995).

¹¹ H. Kuwahara, T. Okuda, Y. Tomioka, A. Asamitsu, and Y. Tokura, *Mat. Res. Oc. Symp. Proc.* **494**, 83 (1998).

¹² H. Kuwahara, T. Okuda, Y. Tomioka, A. Asamitsu, and Y. Tokura, unpublished, and private communications.

¹³ H. Kuwahara, Y. Moritomo, Y. Tomioka, A. Asamitsu, M. Kasai, R. Kumai, and Y. Tokura, *Phys. Rev. B* **56**, 9386 (1997).

¹⁴ F. Izumi, *The Rietveld Method*, ed. by R. A. Young, (Oxford University Press, Oxford, 1993), Chap. 13; Y.-I. Kim and F. Izumi, *J. Ceram. Soc. Jpn.*, **102**, 401 (1994).

¹⁵ Although the relation of the *a* and *b* parameters is reverse to the definition in Ref. 3, we shall call this structure as O' structure in this paper.

¹⁶ Z. Jirák, E. Pollert, A. F. Andersen, J.-C. Grenier, and P. Hagenmuller, *Eur. J. Solid State Inorg. Chem.* **27**, 421 (1990).

¹⁷ V. Caignaert, F. Millange, M. Hervieu, E. Suard, and B. Raveau, *Solid State Comm.* **99**, 173 (1996).

¹⁸ J. Wolfman, A. Maignan, Ch. Simon, and B. Raveau, *J. Magn. Magn. Matt.* **159**, L299 (1996).

¹⁹ A. Sundaresan, P. L. Paulose, R. Mallik, and E. V. Sampathkumaran, *Phys. Rev. B* **57**, 2690 (1998).

²⁰ A. M. Glazer, *Acta Crystallogr. A* **31**, 756 (1975).

²¹ H. Yoshizawa, H. Kawano, Y. Tomioka, and Y. Tokura, *Phys. Rev. B* **52**, R13145 (1995); H. Yoshizawa, H. Kawano, Y. Tomioka, and Y. Tokura, *J. Phys. Soc. Jpn.* **65**, 1043 (1996).

²² R. Kajimoto, T. Kakeshita, Y. Oohara, H. Yoshizawa, Y. Tomioka, and Y. Tokura, *Phys. Rev. B* **58**, R11837 (1998).

²³ D. E. Cox, P. G. Radaelli, M. Marezio, and S-W. Cheong, *Phys. Rev. B* **57**, 3305 (1998).

²⁴ An *metallic* A-type AFM state is also reported by T. Akimoto, Y. Maruyama, Y. Moritomo, A. Nakamura, K. Hirota, K. Ohoyama, and M. Ohashi, *Phys. Rev. B* **57**, R5594 (1998).

²⁵ Y. Moritomo, T. Akimoto, A. Nakamura, K. Ohoyama, and M. Ohashi, *Phys. Rev. B* **58**, 5544 (1998).

²⁶ Close inspection of the crystal structures of the CE-type samples and the A-type $x = 0.55$ sample leads one to notice that there is no significant difference of the structural parameters except a smooth variation as a function of x .

²⁷ H. Yoshizawa, H. Kawano, J. A. Fernandez-Baca, H. Kuwahara, and Y. Tokura, *Phys. Rev. B* **58**, R571 (1998).

²⁸ As far as the diffraction condition is concerned, it is possible that the canting angle is 0° . However, from the value of the magnetic moments listed in Table I, 0° canting angle implies the abnormal moment distribution of $\sim 4\mu_B$ and $\sim 0.9\mu_B$, and it is very unlikely.

²⁹ B. J. Sternlieb, J. P. Hill, U. C. Wildgruber, G. M. Luke, B. Nachumi, Y. Moritomo, and Y. Tokura *Phys. Rev. Lett.* **76**, 2169 (1996).

³⁰ M. Kubota, H. Yoshizawa, H. Fujioka, K. Hirota, Y. Moritomo, and Y. Endoh, *cond-mat/9811192*.

³¹ We noticed that the profiles of several peaks are broad and asymmetric.

³² A. P. Ramirez, P. Schiffer, S-W. Cheong, C. H. Chen, W. Bao, T. T. M. Palstra, P. L. Gammel, D. J. Bishop, and B. Zegarski, *Phys. Rev. Lett.*, **76**, 3188 (1996).

³³ C. H. Chen and S.-W. Cheong, *Phys. Rev. Lett.* **76**, 4042 (1996).

³⁴ C. H. Chen, S-W. Cheong, and H. Y. Hwang, *J. Appl. Phys.* **81**, 4326 (1997).

³⁵ S. Mori, C. H. Chen, and S-W. Cheong, *Nature* **392**, 473 (1998).

³⁶ S. Mori, C. H. Chen, and S-W. Cheong, *Phys. Rev. Lett.* **81**, 3972 (1998).

³⁷ W. Bao, J. D. Axe, C. H. Chen, and S-W. Cheong, *Phys. Rev. Lett.* **78**, 543 (1997).

³⁸ Y. Murakami, D. Shindo, H. Chiba, M. Kikuchi, and Y. Shono, *Phys. Rev. B* **55**, 15043 (1997).

³⁹ M. R. Lees, J. Barratt, G. Balakrishnan, D. McK. Paul, and C. Ritter, *Phys. Rev. B* **58**, 8694 (1998).

⁴⁰ P. G. Radaelli, D. E. Cox, M. Marezio, S-W. Cheong, *Phys. Rev. B* **55**, 3015 (1997); P.G. Radaelli, D.E. Cox, L. Capogna, S-W. Cheong, M. Marezio, *cond-mat/9812366*.

⁴¹ M. R. Ibarra, J. M. De Teresa, J. Blasco, P. A. Algarabel, C. Marquina, J. Garcia, J. Stankiewicz, and C. Ritter, *Phys. Rev. B* **56**, 8252 (1997).